

1    **Title:** Planar cell polarity is essential for the architectural patterning of the mammalian biliary  
2    tree.

3    **Authors:** Michaela Raab<sup>1</sup>, Ersi Christodoulou<sup>1</sup>, Roopesh Krishnankutty<sup>2</sup>, Nicholas T  
4    Younger<sup>1</sup>, Konstantinos Gournopanos<sup>1</sup>, Alexander von Kriegsheim<sup>2</sup>, Scott H Waddell<sup>1</sup>, Luke  
5    Boulter<sup>1, 2</sup>

6

7    **Affiliations:**

8    <sup>1</sup>MRC Human Genetics Unit, Institute of Genetics and Cancer, Edinburgh, EH4 2XU

9    <sup>2</sup>Cancer Research UK Scotland Centre, Edinburgh EH4 2XU

10    **Corresponding author:** Dr Luke Boulter ([luke.boulter@ed.ac.uk](mailto:luke.boulter@ed.ac.uk)).

11

12 **Abstract:** In the developing liver, bipotent epithelial progenitor cells known as hepatoblasts  
13 undergo lineage segregation to form the two major epithelial cell types, hepatocytes that  
14 constitute the bulk of the liver parenchyma and biliary epithelial cells (cholangiocytes) which  
15 comprise the bile duct, a complex tubular network which is critical for normal liver function.  
16 Notch and TGF $\beta$  signalling promote the formation of a sheet of biliary epithelial cells, the ductal  
17 plate that organises into discontinuous tubular structures. How these structures elongate and  
18 connect to form a continuous duct remains undefined. Here, we show that the planar cell  
19 polarity protein, VANGL2 is expressed late in intrahepatic bile duct development and patterns  
20 the formation of cell-cell contacts between biliary cells. The patterning of these cell contacts  
21 regulates the normal polarisation of the actin cytoskeleton within biliary cells and loss of  
22 *Vangl2*-function results in the abnormal distribution of cortical actin remodelling resulting in  
23 the failure of bile duct formation. Planar cell polarity is a critical step in the post-specification  
24 sculpture of the bile duct and is essential for establishing normal tissue architecture.

25 **Keywords:** Duct, Planar Cell Polarity, cell contacts, Van Gogh-like

26 **Introduction:** Intrahepatic bile ducts form in vertebrates from a transient embryological  
27 structure known as the ductal plate that comprises two layers of simple epithelial cells<sup>1</sup>. The  
28 developmental signals that are required to specify the ductal plate from bipotent hepatoblasts  
29 (foetal epithelial progenitor cells in the liver) are well known and deficiencies in both Notch and  
30 TGF $\beta$  signalling in particular are associated with poorly developed, mis-branched or absent  
31 bile ducts<sup>2-5</sup>. Alagille patients who have congenital mutations in *JAGGED1* and less frequently  
32 in *NOTCH2*, for example, suffer from cholestasis and secondary liver disease due to a poorly  
33 formed biliary tree that necessitates non-curative surgery or liver transplantation<sup>6</sup>. Following  
34 specification of the biliary lineage, small stretches of primordial duct must lumenise to form  
35 discontinuous hollow tubes, which then elongate and intercalate to establish the final complex  
36 and branched biliary network<sup>7</sup>. What the molecular processes are that promote the formation  
37 of a continuous, higher-order ductular network from these discontinuous primordial ducts  
38 remains elusive.

39 Across a range of ductular or tubular tissues, including pancreas<sup>8,9</sup>, kidney<sup>10</sup> and lung<sup>11,12</sup>,  
40 planar cell polarity (PCP) signalling is required for the collective polarisation and movement of  
41 epithelial cells. Loss or ectopic activation of PCP signalling is deleterious for normal tubular  
42 architecture, implying that cell-intrinsic levels of PCP components are critical for correct tissue  
43 patterning. In normal mammalian development, PCP proteins (including CELSR, VANGL and  
44 FZD, for example) asymmetrically localise along the proximal-distal axis of cells thereby  
45 imparting spatial information across a population of cells perpendicular to the apico-basal cell  
46 axis<sup>13,14</sup>. Indeed, evidence from zebrafish demonstrated that targeting PCP components *pk1a*,  
47 *vangl2* or *ankrd6* affects the development of a complex biliary tree<sup>15</sup>. While PCP confers a  
48 biochemical gradient across populations of cells within a tissue, how directionality is physically  
49 translated into polarised cellular movements is less clear. The prevailing hypothesis is that  
50 PCP proteins activate intracellular ROCK and RHO-GTPases<sup>16</sup> to coordinate local  
51 cytoskeleton remodelling and cell-cell connectivity<sup>17</sup>.

52 We have previously demonstrated that following adult bile duct damage reactivation of PCP  
53 coordinates bile duct regrowth<sup>18</sup>, a process that recapitulates many of the features of bile duct  
54 ontogeny; therefore, we reasoned that during bile duct development, PCP could represent a  
55 critical factor in embryonic ductular patterning. Using a combination of single cell RNA  
56 sequencing data and a mutant mouse line carrying a hypomorphic mutation in *Vangl2*  
57 (*Vangl2*<sup>S464N</sup>) we demonstrate that the expression of core PCP pathway components is  
58 restricted until late in development when the biliary tree is undergoing morphogenesis and by  
59 patterning cell-cell junctions, PCP drives terminal patterning of the bile duct.

60

61 **Materials and Methods:**

62 **Re-analysis of single cell data from Yang et al:** TPM files were downloaded from GEO and  
63 analysed in R using the Seurat package. Prior to creating a Seurat object, duplicates were  
64 removed and cells were filtered. Cells with a unique feature count over 10,000 or less than  
65 7,000 were removed. Following this, the data was normalised by applying the global-scaling  
66 normalisation method “LogNormalise()” which normalises the feature expression  
67 measurements for each cell by the total expression. The result is then multiplied by a scale  
68 factor of 10,000. Next, highly variable features were identified with the  
69 “FindVariableFeatures()” method, which returned 2000 features that exhibit high cell-to cell  
70 variation in the dataset and were used for downstream analysis. To determine whether cells  
71 cluster according to their cell cycle state, the function “CellCycleScoring” was applied, which  
72 revealed clustering of the cells based on their S- and G2M-Score. To overcome this, cell cycle  
73 regression was performed. Next, the linear transformation function “ScaleData” was applied  
74 to scale the data. This function shifts the expression of each gene so that the mean expression  
75 across the cells is 0 and scales the expression of each gene, such that the variance across  
76 cells is 1. For PCA analysis on the scaled data, the previously determined variable features  
77 were used as an input. To determine the dimensionality of the dataset, the “ElbowPlot()” was  
78 used, which ranks the principal components based on the percentage of variance. The elbow  
79 was found at around PC25-30, hence PC30 was chosen as a cut-off. For clustering the cells,  
80 the functions “FindNeighbours()” and “FindClusters()” were applied using previously defined  
81 dimensionality of the dataset (PC30) as input and at a resolution of 0.5. Non-linear dimensional  
82 reduction the UMAP technique was used, which identified 5 independent clusters. To find  
83 differentially expressed features, the function “FindAllMarkers()” on positive markers was  
84 applied with a minimum percentage of 0.25 and a log fold change threshold of 0.25. To  
85 visualise marker expression, the functions “VlnPlot()”, “FeaturePlot()” and “DotPlot()” were  
86 used.

87 **Animal models:** *Vangl2*<sup>+/GFP</sup> mice were kindly provided by Ping Chen and were maintained  
88 on a CD1 background<sup>19</sup>. *Vangl2*<sup>GFP/GFP</sup> (from hereon in called *Vangl2*<sup>GFP</sup>) embryos were used  
89 at E18.5 and *Vangl2*<sup>+/+</sup> littermates were used as controls *Vangl2*<sup>S464N</sup> mice: *Vangl2*<sup>+/S464N</sup> mice<sup>20</sup>  
90 were provided by Harwell, UK and were maintained on a C3H background. Heterozygous  
91 animals were bred together to generate embryos homozygous for the *Vangl2* mutation,  
92 *Vangl2*<sup>S464N/S464N</sup> (abbreviated to *Vangl2*<sup>S464N</sup>) and *Vangl2*<sup>+/+</sup> controls were maintained on a  
93 C3H background. Embryonic days were counted from day of a found plug (E0.5) for both  
94 mouse lines.

95 Animals were maintained in SPF environment and studies carried out in accordance with the  
96 guidance issued by the Medical Research Council in "Responsibility in the Use of Animals in  
97 Medical Research" (July 1993) and licensed by the Home Office under the Animals (Scientific  
98 Procedures) Act 1986. Experiments were performed under project license number  
99 PFD31D3D4 in facilities at the University of Edinburgh (PEL 60/6025).

100 **Generation of Foetal Liver Organoids (FLO):** Livers were dissected from E15.5 *Vangl2*<sup>+/+</sup>,  
101 *Vangl2*<sup>S464N</sup> or *Vangl2*<sup>eGFP</sup> embryos under sterile conditions. Livers were digested with  
102 collagenase- and dispase-containing digestion buffer and dissociated into single cells.  
103 Pelleted cells were washed in PBS and suspended in 100% matrigel and added to a cell  
104 culture plate. Foetal liver cells were cultured in organoid culture media composed of Advanced  
105 DMEM/F-12 media supplemented with GlutaMAX, Antibiotic-Antimycotic, 10 µM HEPES, 50  
106 ng/ml EGF, 100 ng/ml FGF10, 5 ng/ml HGF, 10 nM gastrin, 10 mM nicotinamide, 1.25 mM N-  
107 acetyl-L-cysteine, 1X B27, 1X N2 Supplement, 10 µM forskolin, 10 µM Y-27632, 5µM A83-01  
108 and 3.33 µM Chir99021.

109 **Mass spectroscopy:** Snap frozen E18.5 livers of *Vangl2*<sup>+/GFP</sup> and *Vangl2*<sup>+/+</sup> mice (N=3 in each  
110 case) were lysed in RIPA lysis buffer supplemented with protease inhibitor. Tissue was  
111 sonicated at 50Hz for 5min using a metal bead for each sample. The lysate was left at 4°C for  
112 30 min to allow for complete cell lysis. Lysate was then centrifuged at 16.000 x g for 20 min at  
113 4°C and protein lysate was transferred to a new tube. Protein concentration was measured by

114 BCA assay. Co-immunoprecipitation pull down experiments (Co-IP) used 500  $\mu$ l of protein  
115 lysate at a concentration of 2 mg/ml in lysis buffer. Co-IP was performed using the Kingsfisher  
116 Flex robot at the in-house mass spectrometry facility using the following protocol. To protein  
117 lysates, magnetic agarose GFP-Trap beads (Chromotek) were added to allow GFP binding to  
118 beads. Beads were washed in lysis buffer and protein eluted with TBS. Proteins were digested  
119 with trypsin and cysteine residues were alkylated with 2-Chloracetamide solution and kept in  
120 the dark. Columns for protein binding were prepared as follows: C18 Discs (Emmore 3M C18)  
121 were punched out using a blunted syringe needle and pushed into 200  $\mu$ l tips before activating  
122 with methanol. Whole protein samples were loaded on to tip columns which were stored until  
123 mass spectrometry. Prior to mass spectrometry, protein was eluted from columns with 50%  
124 acetonitrile, dried and resuspended in 0.1 % TFA/Water and ran on a Lumos Fusion mass  
125 spectrometer coupled to a uHPLC RSLCnano (Thermo Fisher). To identify significantly  
126 enriched proteins, the median of the MaxLFQIntensity of each group (*Vangl2*<sup>eGFP</sup> and  
127 *Vangl2*<sup>+/+</sup>) between the three replicates was taken. The negative log fold change for both  
128 groups was calculated and subtracted from each other. Log fold change values  $>1$  was  
129 considered as significantly enriched. All enriched proteins in the *Vangl2*<sup>eGFP</sup> samples were  
130 used for a downstream gene ontology analysis using the online DAVID and REVIGO platforms  
131 and compared against the *Vangl2*<sup>+/+</sup> control.

132 **Immunostaining of tissues and organoids:** FUnGi tissue clearing<sup>21</sup>: E18.5 livers were  
133 dissected and either cut into thin slices or kept as whole livers and fixed in 4 % PFA. The  
134 tissue was transferred to Washing buffer (WB, PBS + 0.1 % Tween20 + 50  $\mu$ g/ml ascorbic  
135 acid + 0.5 ng/ml reduced L-Glutathione) for 1 h at 4 °C rolling. Tissues were depigmented  
136 using DMSO, 30% H2O and PBS, (ratio of 1:2:4) and washed in Washing buffer 1 (WB1: PBS,  
137 0.2 % Tween, 0.2 % Triton, 0.02 % SDS, 0.2 % BSA, 50  $\mu$ g/ml ascorbic acid, 0.5 ng/ml L-  
138 glutathione reduced). Primary antibodies were diluted in washing buffer 2 (WB2: PBS + 0.1 %  
139 Triton-X-100 + 0.02 % SDS + 0.2 % BSA + 50  $\mu$ g/ml ascorbic acid + 0.5 ng/ml L-Glutathione  
140 reduced) and incubated with tissue overnight. Livers were washed in WB2 and Secondary

141 antibodies were diluted in WB2 (1:500) and incubated with livers ON at 4°C. Tissue was  
142 subsequently washed with WB2 and clarified with FunGI clearing agent (50/50 % v/v glycerol  
143 solution in H<sub>2</sub>O + 10.6 ml Tris Base + 1 mM EDTA + 2.5 M fructose + 2.5 M urea) overnight.  
144 Tissues were mounted on slides for imaging.

145 **IHC and DAB staining:** Dissected tissues were fixed overnight in formalin at 4 °C, embedded  
146 in paraffin and were sectioned at 4 µm. Following antigen retrieval (Supplementary Table 1),  
147 tissue sections were incubated with antibodies as detailed in Supplementary Table 1.  
148 Fluorescently stained tissues were counterstained with DAPI prior to imaging. Colorimetric  
149 stains were counterstained with haematoxylin and mounted with DPX. DAB mean  
150 measurements were quantified using QuPath (<https://qupath.github.io/>). Histological tissues  
151 were scanned using a Nanozoomer, using a Nikon A1R or Leica Stellaris confocal microscope  
152 and were analysed using either FIJI, Imaris, or QuPath. **Organoid Immunofluorescent:**  
153 Organoids were fixed with 4 % Formalin solution in glass-bottom plates. Following  
154 permeabilisation with Triton-X, cells were washed in PBS and glycine (PBS + 100 mM glycine)  
155 and proteins were blocked followed by incubation with primary antibodies, Supplementary  
156 Table 1. Organoids were mounted with Fluromount-G with DAPI prior to imaging.

157 **Electron Microscopy:** Samples were fixed in 3% glutaraldehyde in 0.1 M Sodium Cacodylate  
158 buffer, pH 7.3, for 2 h then washed in three 10 min changes of 0.1 M Sodium Cacodylate.  
159 Specimens were then post-fixed in 1% Osmium Tetroxide in 0.1 M Sodium Cacodylate for 45  
160 min, then washed in three 10 min changes of 0.1M Sodium Cacodylate buffer. These samples  
161 were then dehydrated in 50%, 70%, 90% and 100% ethanol (X3) for 15 min each, then in two  
162 10 min changes in Propylene Oxide. Samples were then embedded in TAAB 812 resin.  
163 Sections, 1 µm thick were cut on a Leica Ultracut ultramicrotome, stained with Toluidine Blue,  
164 and viewed in a light microscope to select suitable areas for investigation. Ultrathin sections,  
165 60nm thick were cut from selected areas, stained in Uranyl Acetate and Lead Citrate then  
166 viewed in a JEOL JEM-1400 Plus TEM. Representative images were collected on a GATAN  
167 OneView camera.

168 **Fluorescent cell membrane labelling:** After establishing single cell suspensions of both  
169 *Vangl2*<sup>+/+</sup> and *Vangl2*<sup>S464N</sup> organoid lines, PKH26 (red) and PKH67 (green) general membrane  
170 dyes were used to label cells as per the manufacturer's instructions. PKH67-labelled *Vangl2*<sup>+/+</sup>  
171 and PKH26-labelled *Vangl2*<sup>S464N</sup> cells were intermixed at a 1:1 ratio, with 20,000 cells in each  
172 well. Additionally, two control wells of PKH67-*Vangl2*<sup>+/+</sup>/PKH26-*Vangl2*<sup>+/+</sup> and PKH67-  
173 *Vangl2*<sup>S464N</sup>/PKH26-*Vangl2*<sup>S464N</sup> were also plated with the same cell density. After 2 days,  
174 images of formed organoids were acquired, and the number of red/green/mosaic organoids  
175 was recorded. A chi-square test was used to assess whether there were significantly  
176 meaningful differences between the three groups.

177 **Immunoblotting:** Protein lysates were obtained from using RPPA lysis buffer (2.5 ml Triton-  
178 X-100, 25 ml 0.5 M HEPES pH 7.4, 0.5 ml 0.5 M EGTA pH 7.5-8.0, 37.5 ml 1 M sodium  
179 chloride, 0.375 ml 1M magnesium chloride, 0.1 ml 100 mM sodium orthovanadate, 1ml 100  
180 mM tetrasodium pyrophosphate, 1 ml 1M sodium fluoride, 1 cOmplete mini EDTA-free  
181 protease inhibitor tablet (Roche), 1 phosphoSTOP phosphatase inhibitor tablet (Roche), 1 ml  
182 glycerol and 1.9 ml dH<sub>2</sub>O). For Western blots, lysates were loaded (7.5-20 µg protein) onto a  
183 4-12% NuPAGE Bis-Tris gel (Thermo Fisher). Protein lysates were reduced with NuPAGE  
184 LDS sample buffer (4x) and NuPAGE Sample Reducing Agent (10x) prior to running. Gels  
185 were run using NuPAGE MOPS SDS Running buffer containing NuPAGE Antioxidant.  
186 Proteins were transferred onto PVDF membrane (Amersham) using NuPAGE Transfer buffer.  
187 Following transfer membranes were either blocked in 5% dried milk (Marvel) in PBST or 5%  
188 BSA (Sigma Aldrich). Membranes were incubated with primary antibodies (Supplementary  
189 Table 1) in 5% BSA (Sigma Aldrich) at 4 °C overnight. Following washing with PBST,  
190 membranes were incubated with HRP-conjugated secondary antibodies (Supplementary  
191 Table 1) in 3% dried milk (Marvel) or 3% BSA (Sigma Aldrich) at room temperature for 1 h.  
192 Following washing, signal was developed using ECL (Pierce) and visualised using Amersham  
193 ImageQuant 800 (Cytiva). Signal was quantified using either FIJI or Image Studio Lite (LI-  
194 COR).

195 **Live imaging of FLOs with/without SiR-actin:** *Vangl2<sup>+/+</sup>* and *Vangl2<sup>S464N</sup>* organoids were  
196 dissociated into single cells and 5,000 cells for each FLO line were plated in organoid growth  
197 media glass bottom slide on a cushion of 1:1 Ultimatrix and PBS. 1  $\mu$ M SiR-actin and 10  $\mu$ M  
198 Verapamil was added to the organoid media. Organoids were imaged for 24 h. In assays  
199 where we assessed organoid growth, single-cell suspension was observed using the Incucyte  
200 S3 machine over a period of one week, and images were taken every 6 hours. Analysis was  
201 performed using the Incucyte S3 software.

202

203 **Results:**

204 **Planar Cell Polarity components are restricted to the ductular lineage in mammalian**  
205 **liver development:** In the mouse, liver development is initiated from the foregut endoderm  
206 and following the formation of a liver bud at E10.5 liver epithelial cells undergo progressive  
207 specification and differentiation into the two principal epithelial cell lineage in the liver,  
208 hepatocytes and biliary epithelial cells (BECs, also known as cholangiocytes)<sup>18,22,23</sup>. Using a  
209 previously published data set in which epithelial cells were isolated using either DLK1 to select  
210 for hepatocellular lineages or EpCAM to enrich ductular cells (Figure 1A) we sought to  
211 determine the regulators of late ductular patterning<sup>24</sup>. Following processing to define the  
212 number of Seurat clusters and regress out the effects of cell cycle (Supplementary Figure 1A-  
213 C), cells clustered into five clusters using Seurat (Figure 1B). Clusters 0, 1 and 3 principally  
214 comprise of foetal hepatoblasts that continue to express a number of hepatoblast genes  
215 including *Lgr5*, *Tbx3* and *Hnf4a*. Cluster 4 are hepatocytes as defined by a number of  
216 hepatocyte markers including *Cps1*, *Cyp2d10* and *Ppara* and cluster 2 is comprised of cells  
217 that express markers of BECs, *Krt7*, *Krt19* and *Spp1* (Supplementary Figure 1D). Cells in  
218 cluster 3, express elevated levels of the master biliary transcription factor *Sox9* and the planar  
219 cell polarity genes *Vangl1* and *Vangl2* (Figure 1C). Cluster 4 also shows high *Vangl2* transcript  
220 levels. Cells within this cluster are made up from the E10.5 liver bud, prior to the initiation of  
221 definitive hepatogenesis.

222 The separation of the ductal plate and subsequent BEC (Biliary Epithelial Cell) lineage from  
223 the hepatocellular one happens at E14.5 in mice and is driven by localised signals from the  
224 portal mesenchyme<sup>25,26</sup>. Beyond E14.5 and following specification, ductular cells undergo  
225 further differentiation and morphogenesis. Segregating the scRNA-seq data by developmental  
226 time showed that within the BEC cluster (cluster 3) there are cells from E14.5-E17.5 (Figure  
227 1D) indicating that this EpCAM-positive population could provide insight into the post-  
228 specification processes that govern bile duct patterning, whereas Cluster 4 (hepatocytes) was  
229 principally made up of E17.5 cells which were isolated based on DLK1. We pooled all EpCAM-

230 positive cells or DLK1-positive cells from each developmental time point and as anticipated  
231 could see the progressive and increasing expression of biliary marker genes *Epcam*, *Sox9*  
232 and *Krt19* only within the EpCAM positive group. Similarly, *Vangl1*, *Vangl2* and *Ror1* were  
233 only transcriptionally increased within this ductular lineage and not in the DLK1-positive  
234 hepatocytes (Figure 1E).

235 VANGL2 is a core regulator of PCP in vertebrates and is functionally dominant over  
236 VANGL1<sup>27</sup>. Furthermore, ROR1 has been shown to functionally interact with VANGL2<sup>28</sup>. We  
237 therefore asked whether *Vangl2* expression specifically is always present in the ductular  
238 lineage or whether its expression is associated with bile duct maturation. *Vangl2*  
239 transcriptional expression does not particularly correlate with *Sox9* mRNA levels (which is  
240 expressed from the point of ductular specification onwards), however it does strongly correlate  
241 with *Krt19* expression, suggesting that *Vangl2* is intimately linked to the maturation of bile  
242 ducts as they undergo morphogenesis and is not simply present for the duration of  
243 ductulogenesis (Figure 1F).

244 **VANGL2 interacts with cell-cell junction proteins in BECs to pattern cell contacts.**

245 Mutations in *Vangl2* are associated with a range of ductular patterning defects across multiple  
246 organs, however, how VANGL2 results in the collective polarisation of cells and patterning of  
247 migration within a tube remains unclear. Using a transgenic mouse line which has GFP fused  
248 to the C-terminus of *Vangl2* (*Vangl2*<sup>GFP</sup>)<sup>29</sup> and whole mount FUnGI imaging we found that GFP  
249 (Green Fluorescent Protein) (and therefore VANGL2) is located at the apico-lateral  
250 membranes of Keratin-19 expressing BECs in E18.5 livers (Figure 2A). The polarisation of  
251 VANGL2 is associated with convergent extension<sup>19,30,31</sup> and as ductular morphogenesis  
252 requires the elongation of primordial ducts into a continuous biliary tree, we hypothesised that  
253 VANGL2 could coordinate the super-cellular architecture of the duct.

254 To understand this further we captured VANGL2 and its binding partners by co-  
255 immunoprecipitation of VANGL2<sup>GFP</sup> from E18.5 embryonic livers and subjected these proteins  
256 to mass-spectroscopic analysis. Unsurprisingly, the top peptide we isolated was VANGL2  
257 following GFP pulldown, however associated with this we also enriched for DSG1A, RCC2,  
258 RAC3, RACK1 and various TUBB peptides (Figure 2B and Supplementary Table 2).  
259 Furthermore, following Gene Ontology analysis of peptides that are co-precipitated with  
260 VANGL2<sup>GFP</sup> we identified that amongst others, groups of peptides associated with  
261 “desmosome organisation”, “protein localisation to cell junctions” and “intermediate filament  
262 organisation” were particularly enriched (Figure 2C). It is possible that during liver  
263 development VANGL2<sup>GFP</sup> is expressed by non-epithelial cell types, therefore we isolated livers  
264 from E15.5 *Vangl2*<sup>GFP</sup> transgenic mice and use these to derive foetal liver organoids (FLOs).  
265 FLOs are generated in a culture medium which selects for a highly purified population of  
266 biliary-lineage cells<sup>32</sup>. Indeed, VANGL2<sup>GFP</sup> is expressed by BECs which comprise the FLOs  
267 and is physically associated with proteins involved in cell adhesion and intermediate filament  
268 organisation (Supplementary Figure 2A, 2B and Supplementary Table 2).  
269 Collectively, these data suggested that VANGL2 can physically interact with cell junction  
270 proteins and pattern the normal formation of cell-cell contacts. Indeed, in a transgenic mouse

271 line that carries a homozygous hypomorphic mutation in *Vangl2* (*Vangl2*<sup>S464N/S464N</sup>, from  
272 hereon in known as *Vangl2*<sup>S464N</sup>) we found significant defects in tight junctions through reduced  
273 expression and distribution of ZO-1 and Occludin (Figure 2D and Supplementary Figure 2C),  
274 adherens junctions (through deregulation of CDH1 patterning, Figure 2E) and loss of  
275 desmosomes when compared to *Vangl2*<sup>+/+</sup> littermate controls (Figure 2F) suggesting that loss  
276 of functional VANGL2 limits the ability of BECs to normally pattern cell-cell contacts during  
277 ductular development.

278 **Loss of VANGL2 function limits the formation of a normal biliary network.** The loss of  
279 functional VANGL2 limits the normal distribution of cell-cell contacts between BECs during  
280 bile duct development (Figure 2) and, while there are no differences in overall liver size  
281 between *Vangl2*<sup>+/+</sup> and *Vangl2*<sup>S464N</sup> livers at E18.5 (Figure 3A), there is a significant reduction  
282 in the number of Keratin-19 positive ducts distributed throughout the tissue at this time point  
283 (Figure 3B). Given our data suggests that the coordination of bile duct morphogenesis by PCP  
284 proteins is a late event in liver development, we sought to determine whether the phenotypes  
285 we see at E18.5 are established earlier in ductular ontogeny or whether they are concordant  
286 with late ductular remodelling and maturation.

287 VANGL2 is dynamically redistributed during the development of other ductular tissues, and  
288 this re-distribution is essential for the establishment of normal tissue function<sup>8</sup>. Upon  
289 commitment to the BEC lineage and the prior to ductular morphogenesis in the liver (at E14.5),  
290 VANGL2 is localised to the basal surface of the cells comprising the ductal plate. By E18.5,  
291 however, VANGL2 is found at the apico-lateral surface of BECs (Figure 3C), reflecting the  
292 expression pattern found with VANGL2<sup>GFP</sup> (Figure 2) and indicating that PCP is established by  
293 this point. Furthermore, when we quantify the differences between Keratin-19 positive bile  
294 ducts at E17.5 and E18.5 in *Vangl2*<sup>+/+</sup> compared to *Vangl2*<sup>S464N</sup> animals we found that while  
295 there are similar numbers of bile ducts between the two genotypes at E17.5 there is a  
296 substantial reduction in bile duct number by E18.5 (Figure 3D and 3E) and the number of  
297 Keratin-19 positive cells within those bile ducts is also significantly reduced (Figure 3F).

298 Keratin-19 is a basic, type-I Keratin that is part of the Keratin-Desmosome scaffold<sup>33</sup> and which  
299 provides structural integrity to epithelial cells. It is possible then that the loss of Keratin-19 in  
300 *Vangl2*<sup>S464N</sup> mutant bile ducts is due to disruption of intermediate filament formation secondary  
301 to desmosome disruption. Indeed, Keratin-19 levels appear higher in *Vangl2*<sup>+/+</sup> livers  
302 compared to *Vangl2*<sup>S464N</sup> (Figure 3D). To rule this out, we immunostained *Vangl2*<sup>+/+</sup> or  
303 *Vangl2*<sup>S464N</sup> livers with SOX9 (a marker of the ductular lineage that is not associated with the  
304 cytoskeleton) and PCNA to quantify the number of proliferating biliary cells. While the number  
305 of SOX9 expressing cells was significantly reduced in *Vangl2*<sup>S464N</sup> mutant livers at E18.5  
306 compared to control animals (Figure 3G) the proportion of proliferative (PCNA-positive) SOX9-  
307 positive biliary cells did not change. However, the ability of SOX9-positive cells to present a  
308 primary cilium into the lumen of the duct (as a proxy for mature BECs) was significantly  
309 impaired when *Vangl2* was mutated (Figure 3H and Supplementary Figure 2D).

310

311 **VANGL2 patterns intracellular tension and coordinates ductular connectivity.** Ductular  
312 growth relies on the collective tubular migration of cells such that a primordial duct grows to  
313 the correct dimension and fuse with an adjacent duct to form a continuous structure<sup>7,34</sup>. To do  
314 this, cells must polarise and remodel their cytoskeletons in order that collective cell movement  
315 is coordinated. Phosphorylation of myosin light chain-2 (MLC2) results in the stabilisation of  
316 actin filaments and changes in cytoskeletal tension. In E18.5 *Vangl2*<sup>+/+</sup> bile ducts pMLC2<sup>S19</sup> is  
317 polarised across the apical-basal axis of ductular cells with higher levels of apical pMLC2<sup>S19</sup>  
318 at the apical surface. In *Vangl2*<sup>S464N</sup> mutant livers at the same developmental time point,  
319 however, pMLC2<sup>S19</sup> is either completely absent from ductular cells or deregulated within these  
320 cells, being present at the apical, lateral and basal parts of biliary cells (Figure 4A and 4B),  
321 furthermore cells which are absent for pMLC2<sup>S19</sup> are typically shorter than their wild-type  
322 counterparts (Figure 4C).

323 PCP-dependent patterning of the cytoskeleton is required for collective cellular migration.  
324 Using whole mount imaging of bile ducts from E18.5 livers we could demonstrate that at this  
325 stage of liver development the bile duct is formed with a complex network of small ducts  
326 connecting to a larger main duct. In *Vangl2*<sup>S464N</sup> embryonic livers, however, this ductular  
327 network does not form correctly, rather imaging showed that a rudimentary biliary tree develops  
328 with small ductules that do not connect to each other nor do they connect to larger ducts. To  
329 quantify these phenotypic differences, we calculated the size of Keratin-19 positive segments  
330 which were significantly smaller in *Vangl2*<sup>S464N</sup> mice than *Vangl2*<sup>+/+</sup> controls (Figure 4E). In  
331 addition to smaller size ducts, we quantified the number of ducts relative to the number of  
332 gaps made by interconnecting ducts to measure “connectedness” of the biliary tree. We found  
333 that there is a significant deficiency in the connections formed between ducts, with more gaps  
334 in the ducts of *Vangl2*<sup>S464N</sup> mutant livers (Figure 4F).

335 **VANGL2 regulates planar cell polarity signalling to promote ductular morphogenesis.**

336 VANGL2 directly interacts with cell-cell junction proteins to pattern normal duct connectivity in  
337 the developing mammalian bile duct through regulation of the BEC cytoskeleton; however,  
338 whether this directly promotes the fusion of discontinuous primordial ductules to form a  
339 continuous biliary structure is difficult to assay *in vivo*. To overcome this, we isolated E15.5  
340 livers from *Vangl2*<sup>+/+</sup> or *Vangl2*<sup>S464N</sup> embryos and following dissociation derived foetal liver  
341 organoids (FLOs) from these livers (Supplementary Figure 3A). Both *Vangl2*<sup>+/+</sup> and  
342 *Vangl2*<sup>S464N</sup> expressed equivalent levels of SOX9 and KRT19 protein (Supplementary Figure  
343 3B) Furthermore, we found that while VANGL2 protein levels in FLOs harbouring the  
344 *Vangl2*<sup>S464N</sup> mutation are significantly reduced, (Figure 5A, and Supplementary Figure 3C)  
345 there is no compensation from VANGL1 (Supplementary Figure 3C). When either *Vangl2*<sup>+/+</sup>  
346 or *Vangl2*<sup>S464N</sup> FLOs are plated as single cells the organoids that form from *Vangl2*<sup>S464N</sup> mutant  
347 cells are significantly smaller than those from wild-type animals (Figure 5B).

348 Based on our *in vivo* data and the growth deficits seen in *Vangl2*<sup>S464N</sup> FLOs, we sought to  
349 determine how FLOs grow. Using time-lapse imaging over the first 6 days of organoid growth,  
350 we found that wildtype FLOs grow by forming small organoids which then fuse to form larger  
351 structures (Supplementary Movie1). We hypothesised then that small *Vangl2*-mutant  
352 organoids either fail to come together and fuse to form larger organoids or the rate of organoid  
353 fusion is significantly reduced in the *Vangl2*<sup>S464N</sup>-mutant. To dissect this, we dissociated either  
354 mutant or wild-type FLOs to single cells and stained these with either PKH26 or PKH67  
355 general membrane markers. *Vangl2*<sup>+/+</sup> and *Vangl2*<sup>S464N</sup> cells were then either admixed  
356 together or admixed with themselves and the number of single colour or dual colour organoids,  
357 which was quantified (Figure 5C) to determine whether *Vangl2*<sup>S464N</sup> cells have an intrinsic  
358 inability to contribute to organoid formation. When FLO cells were mixed in the following  
359 combinations *Vangl2*<sup>+/+:</sup>*Vangl2*<sup>+/+</sup>, *Vangl2*<sup>+/+:</sup>*Vangl2*<sup>S464N</sup> and *Vangl2*<sup>S464N:</sup>*Vangl2*<sup>S464N</sup> we found  
360 no statistically significant differences in the ability of mutant cells to contribute to the formation  
361 of FLOs. When *Vangl2* mutant and wild-type FLO cells were plated as single cells and imaged

362 over time, however, we found that there was a significant lag in growth of FLO derived from  
363 *Vangl2*<sup>S464N</sup> cells suggesting that the rate at which small organoids merge and fuse to form  
364 more substantial FLOs is limited when *Vangl2* is mutated (Figure 5D).

365 VANGL2 coordinates a signalling cascade which results in the activation of signalling through  
366 both ROCK/RHO<sup>16,35</sup> or JNK, which itself regulates actin fibre maturation<sup>36</sup>. Using single cell  
367 RNAseq data from Yang et al (Figure 1) we looked at expression of the three mammalian *Rho*  
368 homologs (*Rhoa*, *Rhob* and *Rhoc*) and *Mapk8* (the gene encoding JNK) within the EpCAM+  
369 BEC lineage. *Rhoa* is expressed early in ductular development, however expression is lost by  
370 the time ducts are undergoing morphogenesis. *Rhob* and *Rhoc* are both expressed at the  
371 transcript level within this lineage, with increasing numbers of cells expressing *Rhoc* from  
372 E15.5. Similarly, the level of *Mapk8* is increased after ductular lineage commitment and during  
373 ductular morphogenesis (Figure 5E). In the adult regenerating bile duct JNK signalling is lost  
374 following functional *Vangl2*-loss<sup>37</sup> similarly, in FLOs the levels of pJNK<sup>T183/Y185</sup> are significantly  
375 decreased (Figure 5F). Furthermore, when we specifically look for levels of RHOC we found  
376 that this is significantly reduced in FLOs derived from *Vangl2*<sup>S464N</sup> mutant mice (Figure 5G).  
377 Given both JNK and RHOC have a role in actin stabilisation and organisation we stained both  
378 *Vangl2*<sup>+/+</sup> and *Vangl2*<sup>S464N</sup> FLOs with the live actin stain, SiR-Actin and imaged them for 24  
379 hours. In *Vangl2*<sup>+/+</sup> organoids, SiR-Actin polarises to the apical (luminal) side of the cells within  
380 the organoids as they grow and merge. In *Vangl2*<sup>S464N</sup> organoids, however, actin is poorly  
381 polarised, often filling the cells (Figure 5H).

382 The failure to connect primordial ductules together ultimately limits a duct from forming,  
383 however, its impact on normal function has not been addressed. The formation of apico-basal  
384 polarity is essential for normal ion and small molecule transport functions in BECs. We  
385 therefore treated *Vangl2*<sup>+/+</sup> or *Vangl2*<sup>S464N</sup> FLOs with Rhodamine123, a fluorescent substrate  
386 of the MDR1 transporter. In *Vangl2*<sup>+/+</sup> FLOs, Rhodamine123 was actively transported into the  
387 lumen of organoids and could be inhibited by co-treatment with an MDR1-inhibitor, verapamil.  
388 This was not the case in *Vangl2*<sup>S464N</sup> mutant FLOs, which showed a significant reduction in

389 their ability to transport Rhodamine123 into the organoid lumen (Supplementary Figure 4A-  
390 D).

391 Collectively our data shows that when the function of the PCP protein VANGL2 is lost,  
392 embryonic biliary cells are no longer able to form normal cell-cell contacts and intracellular  
393 cytoplasmic tension. Failure to develop this biomechanical framework limits the rate at which  
394 primordial ducts can connect to form a complex, functional biliary network.

395 **Discussion:** The mammalian biliary tree necessarily undergoes a number of morphological  
396 rearrangements to transition from a relatively simple epithelial sheet (which constitutes the  
397 ductal plate) into a complex, branched and continuous tubular network that follow the portal  
398 vasculature<sup>7</sup>. Indeed, a number of studies in mice, fish and human have shown that instructive  
399 signals from the vascular endothelium or the mesenchyme surrounding the vasculature are  
400 essential for the specification of the bile duct lineage<sup>2,38–40</sup>. What the post-specification signals  
401 are that regulate the formation of the biliary tree, however, have remained elusive and what  
402 mechanisms promote discontinuous, primordial ductules to elongate and intercalate to form a  
403 continuous ductular network in mammals is not clear<sup>41</sup>. In zebrafish, Ephrin signalling  
404 contributes to normal ductular growth and patterning<sup>42</sup>. Furthermore, studies using  
405 morpholinos against several components of the PCP pathway showed that these proteins are  
406 required for the formation of a normally patterned bile duct network<sup>15</sup> but whether this is true  
407 in mammals and how PCP regulates bile duct development is not known.

408 The formation of a bile duct of the correct length and width is essential for tissue function<sup>43</sup>  
409 and within the liver and other “tubular” tissues, such as the pancreas and kidney, abnormal  
410 patterning of tubules and ducts leads to organ insufficiency<sup>44,45</sup>. Given the essential nature of  
411 tubule and duct formation and organ function, it is unsurprising perhaps that a core group of  
412 highly conserved signals regulate this process in mammals. In tissues where tubular  
413 structures undergo classical branching morphogenesis in a highly stereotyped manner, such  
414 as the pancreas and lung<sup>46,47</sup> changes in *VANGL2* affect the ability of cells to contribute to  
415 normal tissue architecture<sup>48</sup>. Here, we similarly demonstrate that in the bile duct (which does  
416 not undergo classical branching morphogenesis) PCP components are transcriptionally  
417 expressed and their protein products dynamically localise to the apico-lateral membranes of  
418 BECs during ductular morphogenesis. In lung morphogenesis, *Vangl2*-abrogation results in  
419 changes in cytoskeletal mechanics<sup>49</sup>, however, how cellular-level changes in PCP affects  
420 super cellular patterning of tissues is less clear. We show that in addition to the classical role  
421 of *VANGL2* in regulating Rho and Rac signalling (which impinges on remodelling of the

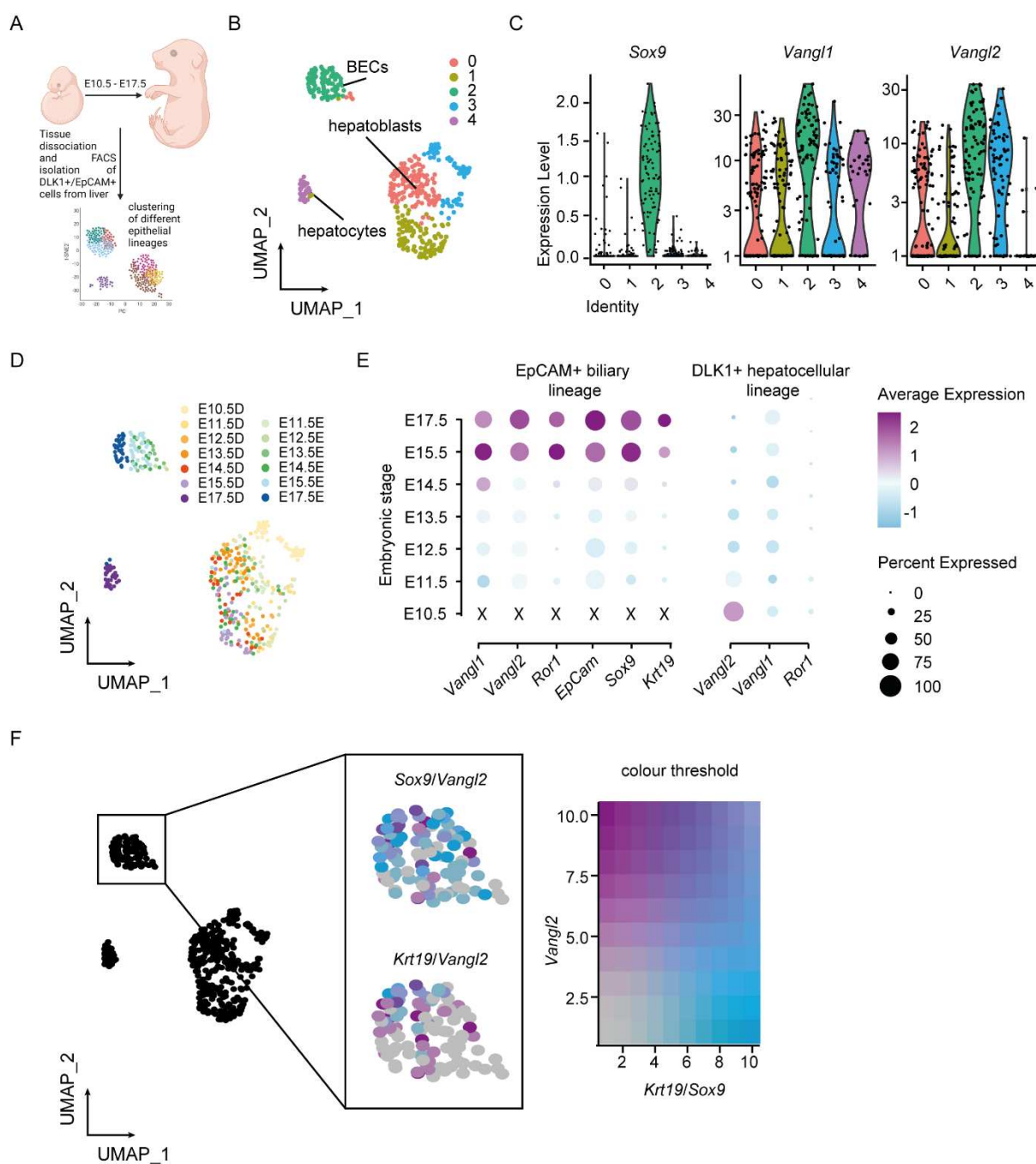
422 cytoskeleton), VANGL2 also physically interacts with proteins that are part of the desmosome  
423 and loss of VANGL2 function results in loss or mis-localisation of cell-cell contacts, which are  
424 themselves essential for providing a group of cells collective directionality<sup>50</sup>.

425 The formation of sophisticated structures is a hallmark of tissue development. This requires  
426 the integration of chemical signals with mechanical tissue-level changes. We demonstrate for  
427 the first time that the mammalian biliary tree relies on planar cell polarity to form correctly  
428 following lineage specification and suggest that this is achieved through patterning of super-  
429 cellular tension within the duct.

430

431 **Acknowledgements:** We would like to thank Matthew Pearson at the IGC (Institute of  
432 Genetics and Cancer) Advanced Imaging Resource, Lizzie Freyer at the IGC Cytometry and  
433 Single Cell Core facility. TEM was provided courtesy of the Wellcome Trust Multiuser  
434 Equipment Grant (WT104915MA) with support from Stephen Mitchell. *Funding:* MR, EC and  
435 NY are funded by an MRC Unit Award. SHW is funded by a Chief Scientist Office (CSO) Early  
436 post-doctoral fellowship (EPD/22/12). A Cancer Research UK Fellowship (C52499/A27948)  
437 funds LB. *Author Contributions:* MR planned and performed experiments, analysed data and  
438 edited the manuscript. EC, RK and NY analysed data and generated figures for the  
439 manuscript. SHW provided intellectual input, experimental design and funding for the project.  
440 LB led the project, funded the project, designed experiments, analysed data, and wrote and  
441 edited the manuscript. *Conflict of Interest:* All authors declare that they have no competing  
442 interests. *Data and materials availability:* All data is available in the manuscript or the  
443 supplementary materials. Single cell RNAseq data from this study is available from:  
444 GSE90047. All materials generated as part of this study will be made available upon request  
445 to the corresponding authors.

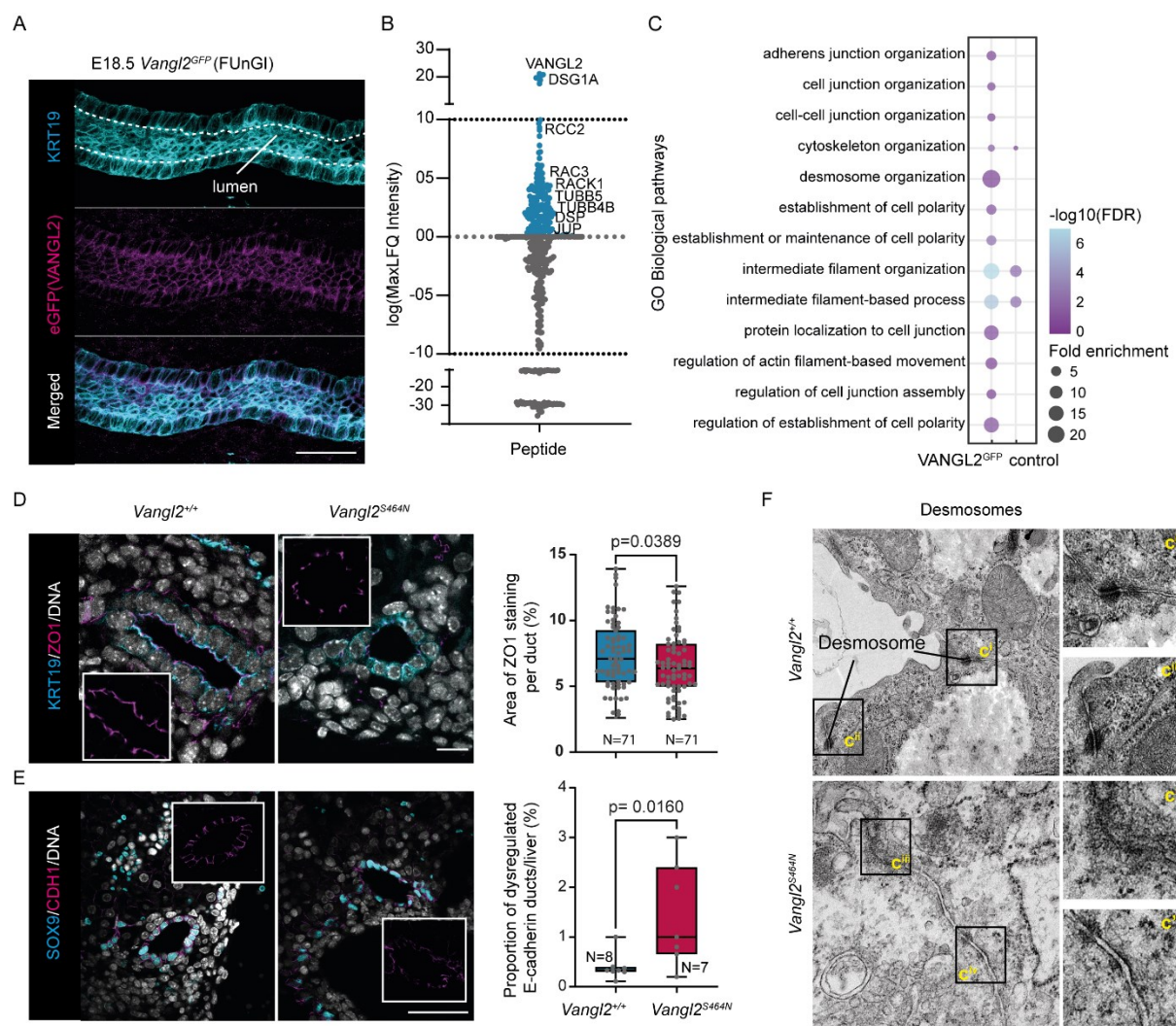
446



447  
448 **Figure 1 – Planar cell polarity pathway components are exclusively expressed in the**  
449 **biliary lineage during liver development. A.** Schematic describing the isolation and scRNA-  
450 seq approach described by Yang et al 2017<sup>24</sup>) of E10.5-E17.5 murine liver. **B.** Seurat  
451 clustering of scRNA-seq data shows 5 distinct clusters (clusters 0-4). **C.** mRNA expression of  
452 the biliary marker, Sox9 and core PCP components *Vangl1* and *Vangl2* between the different  
453 Seurat populations. **D.** Clustered scRNA-seq data coloured by developmental time D denotes  
454 DLK1+ cells and E EpCAM+ cells. **E.** Transcriptional expression of PCP pathway members,  
455 *Vangl1*, *Vangl2* and *Ror1* with the biliary lineage makers *EpCam*, *Sox9* and *Krt19* EPCAM+  
456 cells (left panel) and DLK1+ cells (right panel). **F.** Correlation plot between *Sox9* and *Vangl2*,  
457 and *Krt19* and *Vangl2*.

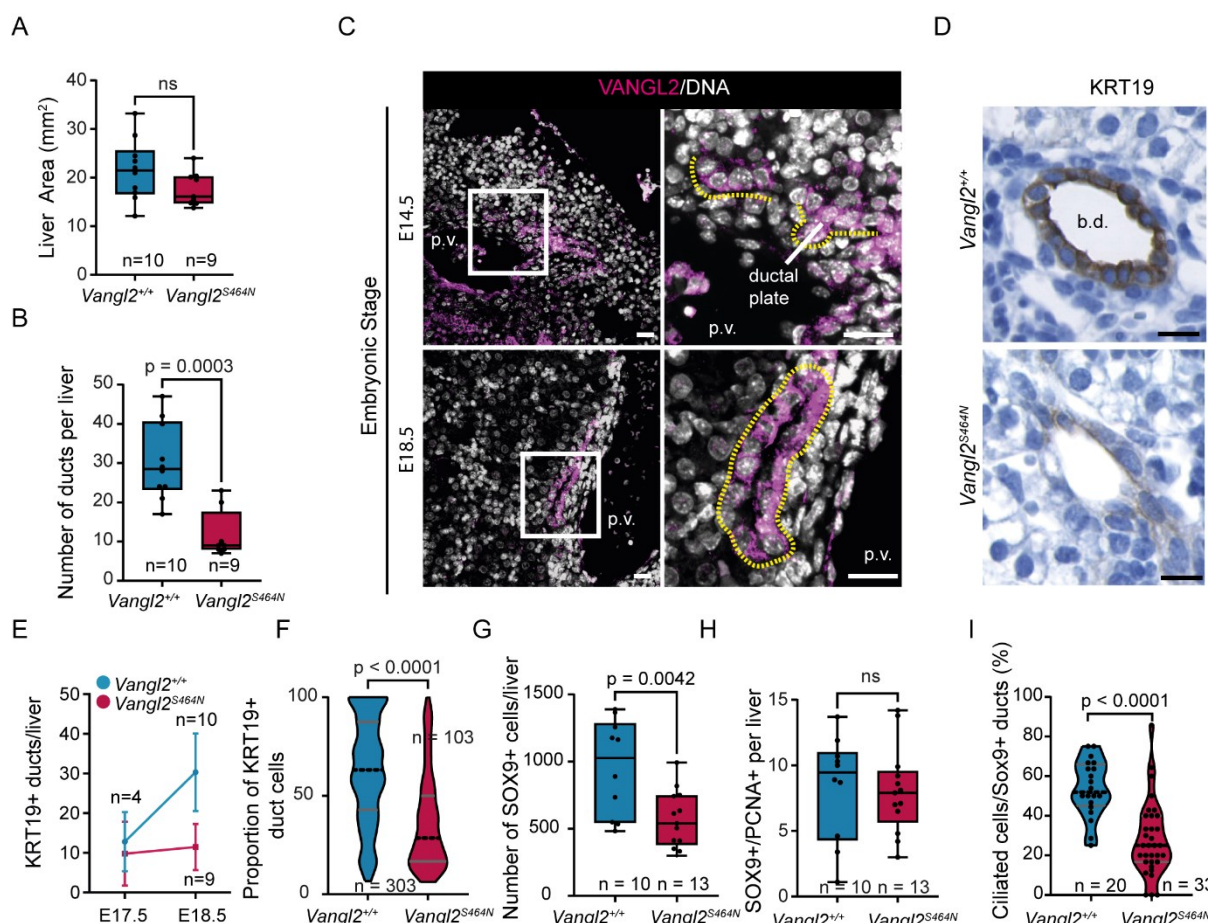
458

459



460  
461 **Figure 2 – VANGL2 interacts with cell-cell junction proteins and coordinates normal**  
462 **junction formation.** **A.** Whole mount imaging of KRT19 positive bile duct (cyan) and GFP (magenta) in VANGL2<sup>GFP</sup> bile ducts. **B.** Peptides found following co-immunoprecipitation mass spectroscopy of VANGL2<sup>GFP</sup> from E18.5 livers when compared to pull down from *Vangl2*<sup>+/+</sup> livers (N=3 biological replicates per condition). **C.** GO Biological Pathway analysis of peptides enriched following co-immunoprecipitation mass spectroscopy **D.** Immunostaining of the biliary marker KRT19 (cyan) and tight junction protein, ZO1 (magenta) in *Vangl2*<sup>+/+</sup> vs *Vangl2*<sup>S464N</sup> livers (scale bar = 15 μm). Histogram, right shows the area of ZO-1 staining within SOX9-positive cells. **E.** Immunostaining of the biliary marker SOX9 (cyan) and adherens junction protein, CDH1 (magenta) in *Vangl2*<sup>+/+</sup> vs *Vangl2*<sup>S464N</sup> livers (scale bar = 50 μm), DNA in white. Histogram, shows the number of ducts with dysregulated CDH1 in *Vangl2*<sup>+/+</sup> vs *Vangl2*<sup>S464N</sup> livers. **F.** Electron micrographs of liver cells from in *Vangl2*<sup>+/+</sup> vs *Vangl2*<sup>S464N</sup> livers.

463  
464  
465  
466  
467  
468  
469  
470  
471  
472  
473  
474

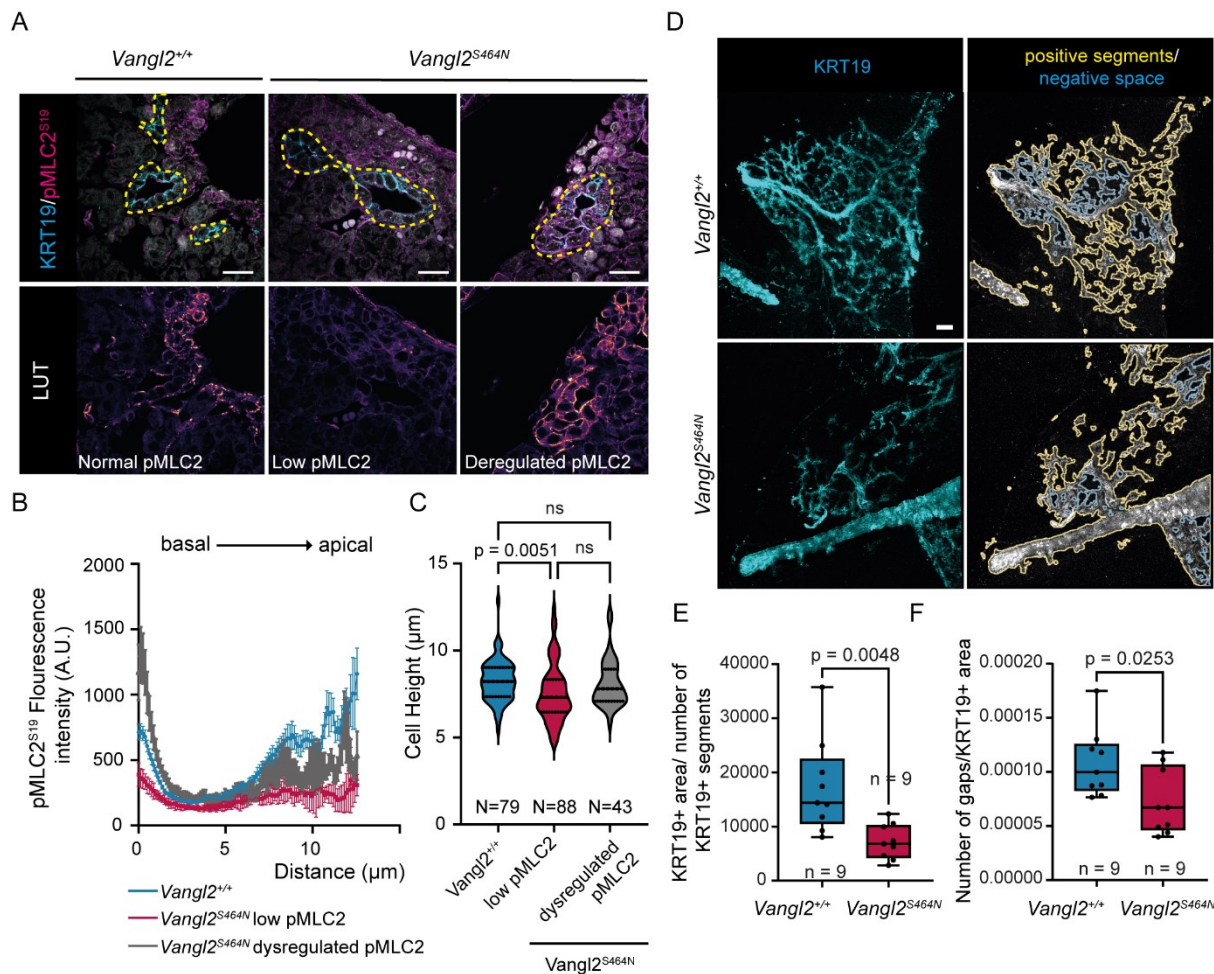


475

**Figure 3 - Mice with hypomorphic *Vangl2*<sup>S464N</sup> do not have a normal biliary tree. A.** Quantification of liver area in E18.5 *Vangl2*<sup>+/+</sup> and *Vangl2*<sup>S464N</sup> livers. **B.** Number of KRT19-positive bile ducts per liver in E18.5 *Vangl2*<sup>+/+</sup> and *Vangl2*<sup>S464N</sup> livers. **C.** VANGL2 immunostaining (magenta) of E14.5 ductal plate cells and E18.5 bile ducts from *VANGL2*<sup>+/+</sup> mice (scale bar = 50µm), DNA grey. Basal surface of the cells demarcated with dotted yellow line. **D.** Immunohistochemistry for KRT19 in *Vangl2*<sup>+/+</sup> and *Vangl2*<sup>S464N</sup> livers (scale bar = 50µm). **E.** Change in the number of KRT19-positive ducts in *Vangl2*<sup>+/+</sup> and *Vangl2*<sup>S464N</sup> livers between E17.5 and E18.5. **F.** H-score (intensity) of KRT19 in ductular cells in *Vangl2*<sup>+/+</sup> and *Vangl2*<sup>S464N</sup> livers at E18.5. **G.** Total number of SOX9-positive cells and **H.** number of proliferating (PCNA-positive) SOX9-positive cells per liver. **I.** Quantification of SOX9-positive bile duct cells presenting a primary cilium (demarcated with AcTUB and ARL13B) in *Vangl2*<sup>+/+</sup> and *Vangl2*<sup>S464N</sup>.

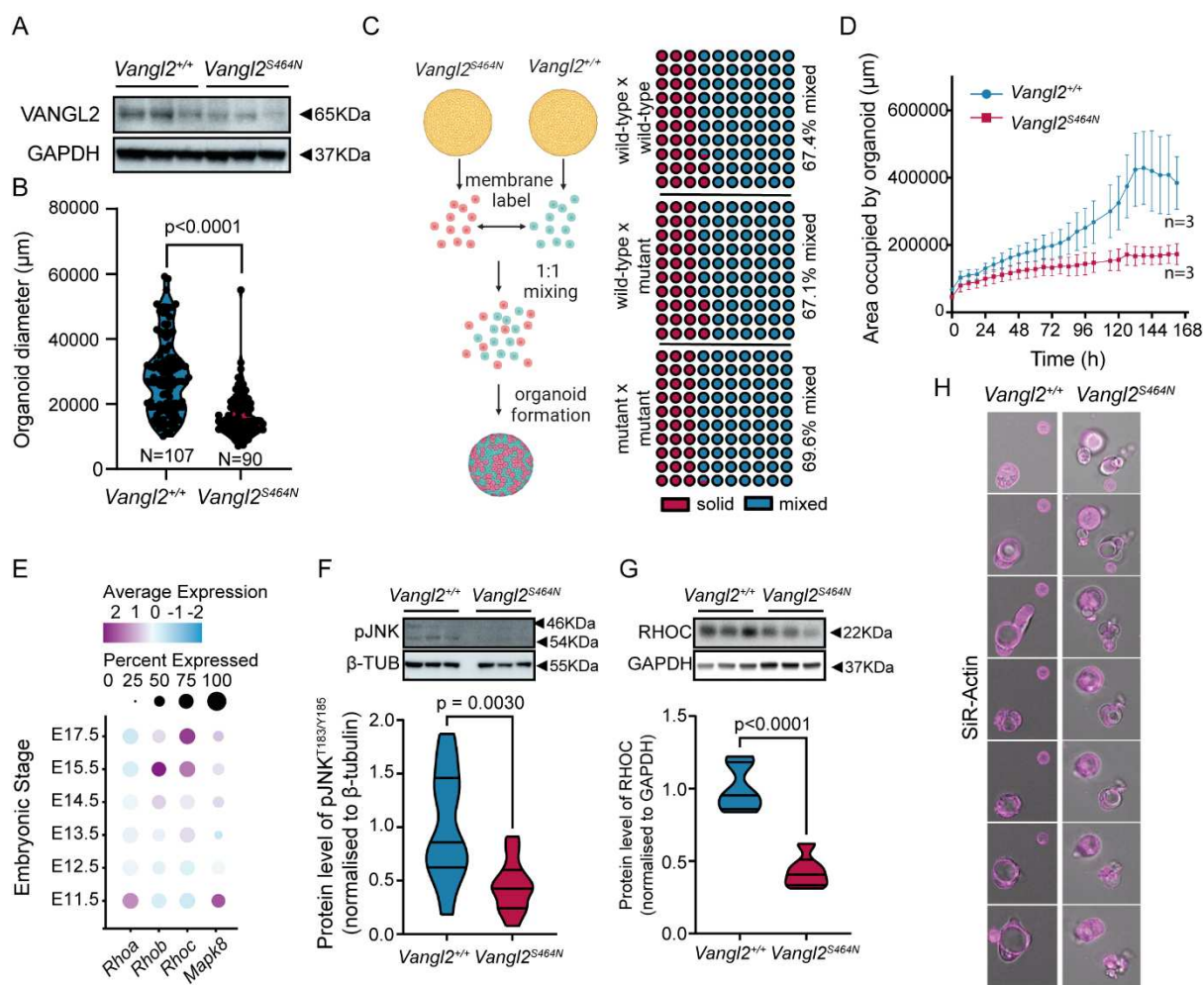
488

489



490

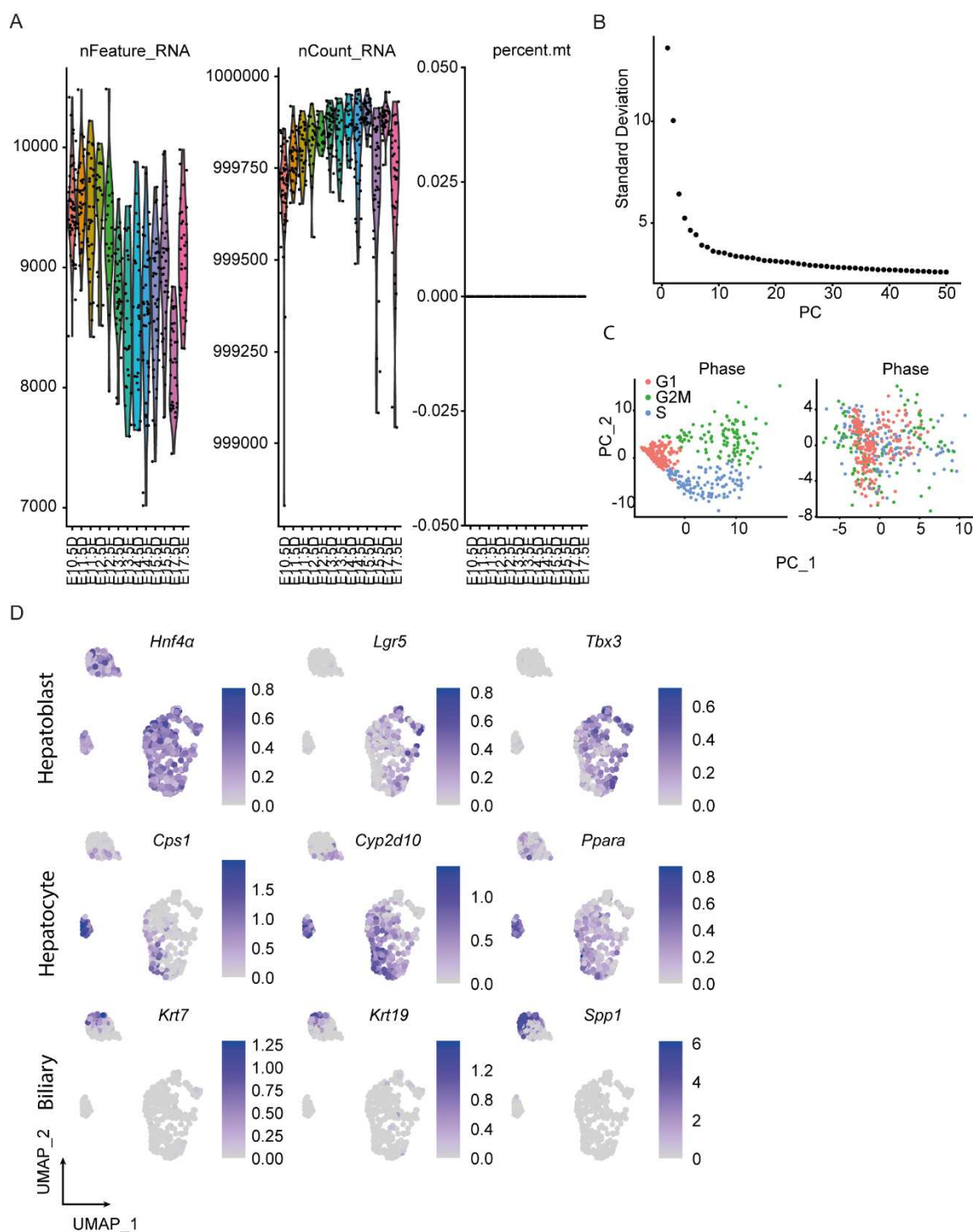
491 **Figure 4 –Loss of functional VANGL2 changes the tertiary structure of bile ducts. A.**  
492 E18.5 *Vangl2*<sup>+/+</sup> and *Vangl2*<sup>S464N</sup> livers immunostained for KRT19 (cyan) and pMLC2<sup>S19</sup>  
493 (magenta), scale bar = 50μm, DNA in white. Lower panels show pMLC2<sup>S19</sup> intensity. **B.**  
494 Quantification of pMLC2<sup>S19</sup> signal intensity along the apico-basal axis of biliary cells in E18.5  
495 *Vangl2*<sup>+/+</sup> (blue line), and in *Vangl2*<sup>S464N</sup> mutant animals with low pMLC2<sup>S19</sup> (magenta)  
496 or dysregulated (mislocalised) pMLC2<sup>S19</sup> (grey). **C.** Cell height of biliary cells from E18.5  
497 *Vangl2*<sup>+/+</sup> and *Vangl2*<sup>S464N</sup> livers. **D.** Whole mount immunostaining for KRT19 (cyan) in  
498 *Vangl2*<sup>+/+</sup> and *Vangl2*<sup>S464N</sup> (left panels), annotations of positive segments and negative space  
499 (right panels). **E, F.** Quantification of bile duct connectivity in E18.5 *Vangl2*<sup>+/+</sup> and *Vangl2*<sup>S464N</sup>  
500 animals.



502 **Figure 5 - VANGL2 promotes ductular-connectivity through actin-regulation. A.**  
503 Immunoblot for VANGL2 and the housekeeping protein GAPDH in *Vangl2<sup>+/+</sup>* and *Vangl2<sup>S464N</sup>*  
504 organoids derived from E14.5 livers. **B.** Diameter of organoids derived from E14.5 *Vangl2<sup>+/+</sup>*  
505 and *Vangl2<sup>S464N</sup>* livers dissociated into single cells and allowed to form. **C.** Schematic and  
506 quantification of organoid admixing from *Vangl2<sup>+/+</sup>* and *Vangl2<sup>S464N</sup>* cells. Red circles denote  
507 organoids comprising of a single colour and blue circles organoids comprising two colours. (N  
508 of organoids analysed: wild-type x wildtype: 406, wild-type x *Vangl2<sup>S464N</sup>*: 420, *Vangl2<sup>S464N</sup>* x  
509 *Vangl2<sup>S464N</sup>*: 485). **D.** Growth of *Vangl2<sup>+/+</sup>* (blue line) *Vangl2<sup>S464N</sup>* (magenta line) single cells  
510 into organoids over 162h **E.** scRNA-seq from EpCAM-positive cells showing transcriptional  
511 levels of *Rhoa*, *Rhob*, *Rhoc* and *Mapk8*. **F.** Immunoblot and quantification of pJNK<sup>T183/Y185</sup> in  
512 organoids derived from *Vangl2<sup>+/+</sup>* and *Vangl2<sup>S464N</sup>* E14.5 organoids. **G.** Immunoblot and  
513 quantification of RHOC in organoids derived from *Vangl2<sup>+/+</sup>* and *Vangl2<sup>S464N</sup>* E14.5 organoids.  
514 **H.** Live imaging of SiR-Actin (magenta) in E14.5 organoids derived *Vangl2<sup>+/+</sup>* and *Vangl2<sup>S464N</sup>*  
515 livers (over 24 hours).

516

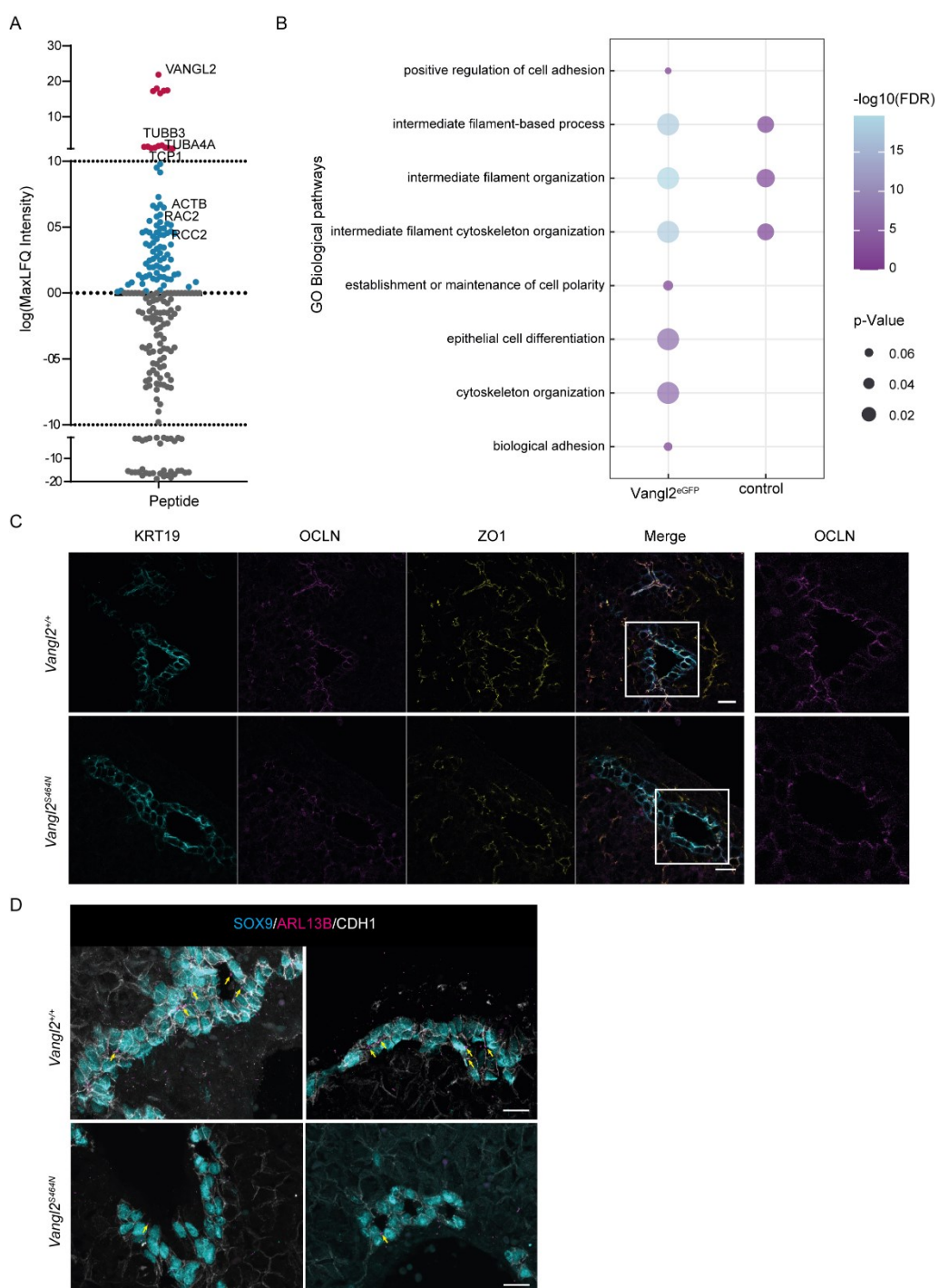
517



518

519 **Supplementary Figure 1: Single cell RNA sequencing identifies changes in gene expression**  
520 **over developmental time.** **A.** Single cell RNA sequencing data from Yang et al. Processed to  
521 show nFeature, nCount and mitochondrial contamination. **B.** Elbow plot to define the number  
522 of clusters used by Seurat to partition the data. **C.** Representation of the data prior to and  
523 following the regressing out of cell cycle effects. **D.** Lineage specific markers of Hepatoblasts  
524 (Hnf4a, Lgr5 and Tbx3), Hepatocytes (Cps1, Cyp2d10 and Ppara) and BECs (Krt7, Krt19 and  
525 Spp1).

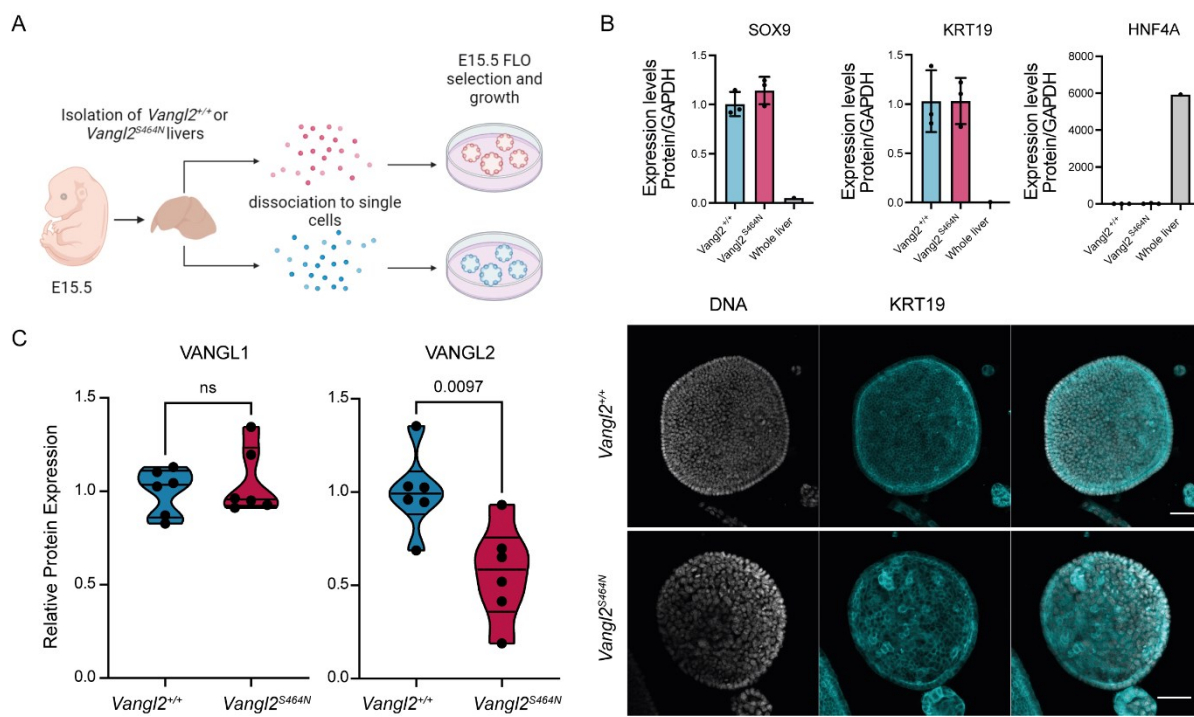
526



527

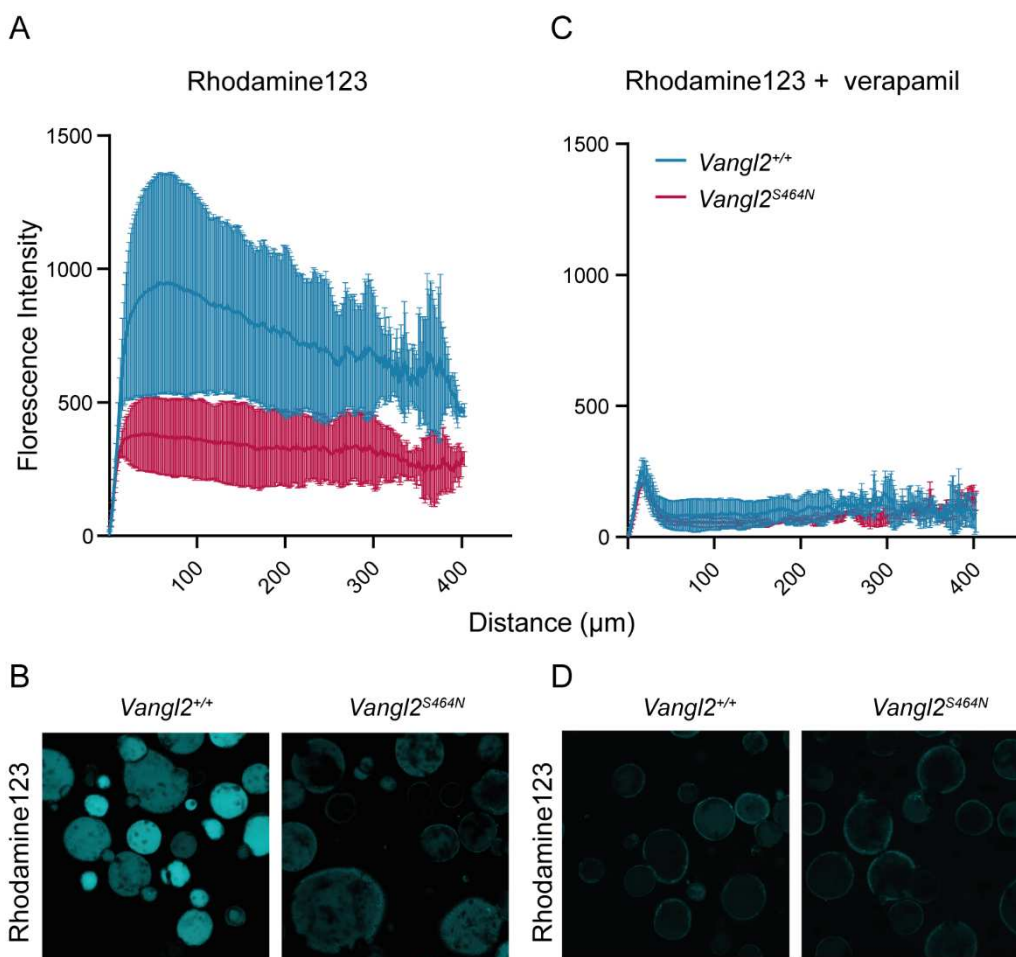
528 **Supplementary Figure 2: VANGL2 is associated with cell-cell junctional stability in BECs. A.**  
529 Significantly enriched peptides following VANGL2<sup>GFP</sup> pulldown and mass spectroscopy from  
530 *Vangl2<sup>GFP</sup>* FLOs compared to *Vangl2<sup>+/+</sup>* FLOs. **B.** Enriched GOTerms for peptides isolated  
531 from co-IP mass spectrometry of VANGL2<sup>GFP</sup> bait. **C.** Immunofluorescent staining of BECs  
532 with KRT19 (cyan) and TJ proteins OCLN (magenta) and ZO1 (yellow) in *Vangl2<sup>+/+</sup>* and  
533 *Vangl2<sup>S464N</sup>* livers at E18.5. Scale bar = 20 $\mu$ m. Insets identify regions which are shown in right  
534 panels. **D.** Immunofluorescent staining of E18.5 SOX9-positive biliary cells (cyan) from  
535 *Vangl2<sup>+/+</sup>* and *Vangl2<sup>S464N</sup>* stained for the AJ protein, CDH1 (white) and the primary cilia  
536 marker, ARL13B (magenta). Scale bar = 20 $\mu$ m.

537



538 **Supplementary Figure 3: Generating FLOs from *Vangl2*<sup>S464N</sup> mutant livers** **A.** A schematic representation of the derivation of *Vangl2*<sup>+/+</sup> and *Vangl2*<sup>S464N</sup> FLOs. **B.** mRNA expression of *Sox9*, *Krt19* and *Hnf4a* (upper panels) in *Vangl2*<sup>+/+</sup> and *Vangl2*<sup>S464N</sup> FLOs compared to whole wild-type liver (N=3 per group, except whole liver where N=1). Lower panels show immunostaining for *KRT19* (cyan) in *Vangl2*<sup>+/+</sup> and *Vangl2*<sup>S464N</sup> FLOs. DNA is represented in white. Scale bar = 50 $\mu$ m. **C.** Quantification of immunoblots for *VANGL1* and *VANGL2* from proteins isolated from *Vangl2*<sup>+/+</sup> and *Vangl2*<sup>S464N</sup> FLOs (N=6).

546



553 **References:**

- 554 1. Tanimizu, N., Miyajima, A., and Mostov, K.E. (2009). Liver progenitor cells fold up a  
555 cell monolayer into a double-layered structure during tubular morphogenesis. *Mol.*  
556 *Biol. Cell* **20**, 2486–2494. 10.1091/mbc.e08-02-0177.
- 557 2. Li, L., Krantz, I.D., Deng, Y., Genin, A., Banta, A.B., Collins, C.C., Qi, M., Trask, B.J.,  
558 Kuo, W.L., Cochran, J., et al. (1997). Alagille syndrome is caused by mutations in  
559 human Jagged1, which encodes a ligand for Notch1. *Nat. Genet.* **16**, 243–251.  
560 10.1038/ng0797-243.
- 561 3. McDaniell, R., Warthen, D.M., Sanchez-Lara, P.A., Pai, A., Krantz, I.D., Piccoli, D.A.,  
562 and Spinner, N.B. (2006). NOTCH2 mutations cause Alagille syndrome, a  
563 heterogeneous disorder of the notch signaling pathway. *Am. J. Hum. Genet.* **79**, 169–  
564 173. 10.1086/505332.
- 565 4. Clotman, F., Jacquemin, P., Plumb-Rudewiez, N., Pierreux, C.E., Van der Smissen,  
566 P., Dietz, H.C., Courtoy, P.J., Rousseau, G.G., and Lemaigre, F.P. (2005). Control of  
567 liver cell fate decision by a gradient of TGF beta signaling modulated by Onecut  
568 transcription factors. *Genes Dev.* **19**, 1849–1854. 10.1101/gad.340305.
- 569 5. Plumb-Rudewiez, N., Clotman, F., Strick-Marchand, H., Pierreux, C.E., Weiss, M.C.,  
570 Rousseau, G.G., and Lemaigre, F.P. (2004). Transcription factor HNF-6/OC-1 inhibits  
571 the stimulation of the HNF-3alpha/Foxa1 gene by TGF-beta in mouse liver.  
572 *Hepatology* **40**, 1266–1274. 10.1002/hep.20459.
- 573 6. Heinz, N., and Vittorio, J. (2023). Treatment of cholestasis in infants and young  
574 children. *Curr. Gastroenterol. Rep.* 10.1007/s11894-023-00891-8.
- 575 7. Tanimizu, N., Kaneko, K., Itoh, T., Ichinohe, N., Ishii, M., Mizuguchi, T., Hirata, K.,  
576 Miyajima, A., and Mitaka, T. (2016). Intrahepatic bile ducts are developed through  
577 formation of homogeneous continuous luminal network and its dynamic  
578 rearrangement in mice. *Hepatology* **64**, 175–188. 10.1002/hep.28521.
- 579 8. Flasse, L., Yenek, S., Cortijo, C., Barandiaran, I.S., Kraus, M.R.-C., and Grapin-  
580 Botton, A. (2020). Apical restriction of the planar cell polarity component VANGL in  
581 pancreatic ducts is required to maintain epithelial integrity. *Cell Rep.* **31**, 107677.  
582 10.1016/j.celrep.2020.107677.
- 583 9. Cortijo, C., Gouzi, M., Tissir, F., and Grapin-Botton, A. (2012). Planar cell polarity  
584 controls pancreatic beta cell differentiation and glucose homeostasis. *Cell Rep.* **2**,  
585 1593–1606. 10.1016/j.celrep.2012.10.016.
- 586 10. Yates, L.L., Papakrivopoulou, J., Long, D.A., Goggolidou, P., Connolly, J.O., Woolf,  
587 A.S., and Dean, C.H. (2010). The planar cell polarity gene Vangl2 is required for  
588 mammalian kidney-branching morphogenesis and glomerular maturation. *Hum. Mol.*  
589 *Genet.* **19**, 4663–4676. 10.1093/hmg/ddq397.
- 590 11. Akram, K.M., Yates, L.L., Mongey, R., Rothery, S., Gaboriau, D.C.A., Sanderson, J.,  
591 Hind, M., Griffiths, M., and Dean, C.H. (2019). Live imaging of alveologenesis in  
592 precision-cut lung slices reveals dynamic epithelial cell behaviour. *Nat. Commun.* **10**,  
593 1178. 10.1038/s41467-019-09067-3.
- 594 12. Yates, L.L., Schnatwinkel, C., Murdoch, J.N., Bogani, D., Formstone, C.J.,  
595 Townsend, S., Greenfield, A., Niswander, L.A., and Dean, C.H. (2010). The PCP

596 genes *Celsr1* and *Vangl2* are required for normal lung branching morphogenesis.  
597 *Hum. Mol. Genet.* 19, 2251–2267. 10.1093/hmg/ddq104.

598 13. Stahley, S.N., Basta, L.P., Sharan, R., and Devenport, D. (2021). *Celsr1* adhesive  
599 interactions mediate the asymmetric organization of planar polarity complexes. *eLife*  
600 10. 10.7554/eLife.62097.

601 14. Cetera, M., Sharan, R., Hayward-Lara, G., Phillips, B., Biswas, A., Halley, M., Beall,  
602 E., vonHoldt, B., and Devenport, D. (2023). Region-specific reversal of epidermal  
603 planar polarity in the rosette fancy mouse. *Development* 150. 10.1242/dev.202078.

604 15. Cui, S., Capecci, L.M., and Matthews, R.P. (2011). Disruption of planar cell polarity  
605 activity leads to developmental biliary defects. *Dev. Biol.* 351, 229–241.  
606 10.1016/j.ydbio.2010.12.041.

607 16. McGreevy, E.M., Vijayraghavan, D., Davidson, L.A., and Hildebrand, J.D. (2015).  
608 *Shroom3* functions downstream of planar cell polarity to regulate myosin II distribution  
609 and cellular organization during neural tube closure. *Biol. Open* 4, 186–196.  
610 10.1242/bio.20149589.

611 17. Krneta-Stankic, V., Corkins, M.E., Paulucci-Holthauzen, A., Kloc, M., Gladden, A.B.,  
612 and Miller, R.K. (2021). The *Wnt/PCP* formin *Daam1* drives cell-cell adhesion during  
613 nephron development. *Cell Rep.* 36, 109340. 10.1016/j.celrep.2021.109340.

614 18. Wilson, D.H., Jarman, E.J., Mellin, R.P., Wilson, M.L., Waddell, S.H., Tsokkou, P.,  
615 Younger, N.T., Raven, A., Bhalla, S.R., Noll, A.T.R., et al. (2020). Non-canonical *Wnt*  
616 signalling regulates scarring in biliary disease via the planar cell polarity receptors.  
617 *Nat. Commun.* 11, 445. 10.1038/s41467-020-14283-3.

618 19. Qian, D., Jones, C., Rzadzinska, A., Mark, S., Zhang, X., Steel, K.P., Dai, X., and  
619 Chen, P. (2007). *Wnt5a* functions in planar cell polarity regulation in mice. *Dev. Biol.*  
620 306, 121–133. 10.1016/j.ydbio.2007.03.011.

621 20. Chen, B., Mao, H.H., Chen, L., Zhang, F.L., Li, K., and Xue, Z.F. (2013). Loop-tail  
622 phenotype in heterozygous mice and neural tube defects in homozygous mice result  
623 from a nonsense mutation in the *Vangl2* gene. *Genet. Mol. Res.* 12, 3157–3165.  
624 10.4238/2013.January.22.2.

625 21. Rios, A.C., Capaldo, B.D., Vaillant, F., Pal, B., van Ineveld, R., Dawson, C.A., Chen,  
626 Y., Nolan, E., Fu, N.Y., 3DTCLSM Group, et al. (2019). Intraclonal Plasticity in  
627 Mammary Tumors Revealed through Large-Scale Single-Cell Resolution 3D Imaging.  
628 *Cancer Cell* 35, 953. 10.1016/j.ccr.2019.05.011.

629 22. Pepe-Mooney, B.J., Dill, M.T., Alemany, A., Ordovas-Montanes, J., Matsushita, Y.,  
630 Rao, A., Sen, A., Miyazaki, M., Anakk, S., Dawson, P.A., et al. (2019). Single-Cell  
631 Analysis of the Liver Epithelium Reveals Dynamic Heterogeneity and an Essential  
632 Role for YAP in Homeostasis and Regeneration. *Cell Stem Cell* 25, 23–38.e8.  
633 10.1016/j.stem.2019.04.004.

634 23. Pu, W., Zhu, H., Zhang, M., Pikolek, M., Ercan, C., Li, J., Huang, X., Han, X., Zhang,  
635 Z., Lv, Z., et al. (2023). Bipotent transitional liver progenitor cells contribute to liver  
636 regeneration. *Nat. Genet.* 55, 651–664. 10.1038/s41588-023-01335-9.

637 24. Yang, L., Wang, W.-H., Qiu, W.-L., Guo, Z., Bi, E., and Xu, C.-R. (2017). A single-cell  
638 transcriptomic analysis reveals precise pathways and regulatory mechanisms  
639 underlying hepatoblast differentiation. *Hepatology* 66, 1387–1401.  
640 10.1002/hep.29353.

641 25. Hofmann, J.J., Zovein, A.C., Koh, H., Radtke, F., Weinmaster, G., and Iruela-Arispe,  
642 M.L. (2010). Jagged1 in the portal vein mesenchyme regulates intrahepatic bile duct  
643 development: insights into Alagille syndrome. *Development* 137, 4061–4072.  
644 10.1242/dev.052118.

645 26. Ader, T., Norel, R., Levoci, L., and Rogler, L.E. (2006). Transcriptional profiling  
646 implicates TGFbeta/BMP and Notch signaling pathways in ductular differentiation of  
647 fetal murine hepatoblasts. *Mech. Dev.* 123, 177–194. 10.1016/j.mod.2005.10.003.

648 27. Dreyer, C.A., VanderVorst, K., and Carraway, K.L. (2022). Vangl as a master scaffold  
649 for wnt/planar cell polarity signaling in development and disease. *Front. Cell Dev. Biol.*  
650 10, 887100. 10.3389/fcell.2022.887100.

651 28. Gao, B., Song, H., Bishop, K., Elliot, G., Garrett, L., English, M.A., Andre, P.,  
652 Robinson, J., Sood, R., Minami, Y., et al. (2011). Wnt signaling gradients establish  
653 planar cell polarity by inducing Vangl2 phosphorylation through Ror2. *Dev. Cell* 20,  
654 163–176. 10.1016/j.devcel.2011.01.001.

655 29. Li, S., Esterberg, R., Lachance, V., Ren, D., Radde-Gallwitz, K., Chi, F., Parent, J.-L.,  
656 Fritz, A., and Chen, P. (2011). Rack1 is required for Vangl2 membrane localization  
657 and planar cell polarity signaling while attenuating canonical Wnt activity. *Proc Natl  
658 Acad Sci USA* 108, 2264–2269. 10.1073/pnas.1013170108.

659 30. Chacon-Heszele, M.F., Ren, D., Reynolds, A.B., Chi, F., and Chen, P. (2012).  
660 Regulation of cochlear convergent extension by the vertebrate planar cell polarity  
661 pathway is dependent on p120-catenin. *Development* 139, 968–978.  
662 10.1242/dev.065326.

663 31. Torban, E., Wang, H.-J., Groulx, N., and Gros, P. (2004). Independent mutations in  
664 mouse Vangl2 that cause neural tube defects in looptail mice impair interaction with  
665 members of the Dishevelled family. *J. Biol. Chem.* 279, 52703–52713.  
666 10.1074/jbc.M408675200.

667 32. Huch, M., Dorrell, C., Boj, S.F., van Es, J.H., Li, V.S.W., van de Wetering, M., Sato,  
668 T., Hamer, K., Sasaki, N., Finegold, M.J., et al. (2013). In vitro expansion of single  
669 Lgr5+ liver stem cells induced by Wnt-driven regeneration. *Nature* 494, 247–250.  
670 10.1038/nature11826.

671 33. Green, K.J., Niessen, C.M., Rübsam, M., Perez White, B.E., and Broussard, J.A.  
672 (2022). The Desmosome-Keratin Scaffold Integrates ErbB Family and Mechanical  
673 Signaling to Polarize Epidermal Structure and Function. *Front. Cell Dev. Biol.* 10,  
674 903696. 10.3389/fcell.2022.903696.

675 34. Xi, W., Sonam, S., Beng Saw, T., Ladoux, B., and Teck Lim, C. (2017). Emergent  
676 patterns of collective cell migration under tubular confinement. *Nat. Commun.* 8, 1517.  
677 10.1038/s41467-017-01390-x.

678 35. Phillips, H.M., Hildreth, V., Peat, J.D., Murdoch, J.N., Kobayashi, K., Chaudhry, B.,  
679 and Henderson, D.J. (2008). Non-cell-autonomous roles for the planar cell polarity  
680 gene Vangl2 in development of the coronary circulation. *Circ. Res.* 102, 615–623.  
681 10.1161/CIRCRESAHA.107.160861.

682 36. Homsy, J.G., Jasper, H., Peralta, X.G., Wu, H., Kiehart, D.P., and Bohmann, D.  
683 (2006). JNK signaling coordinates integrin and actin functions during Drosophila  
684 embryogenesis. *Dev. Dyn.* 235, 427–434. 10.1002/dvdy.20649.

685 37. Wilson, D.H., Mellin, R.P., Younger, N.T., Jarman, E.J., Raven, A., Chen, P., Dean, C., Henderson, D., Kendall, T., and Boulter, L. (2018). Non-canonical Wnt signalling initiates scarring in biliary disease. *BioRxiv*. 10.1101/276196.

688 38. Lorent, K., Moore, J.C., Siekmann, A.F., Lawson, N., and Pack, M. (2010). Reiterative use of the notch signal during zebrafish intrahepatic biliary development. *Dev. Dyn.* 239, 855–864. 10.1002/dvdy.22220.

691 39. Zhang, D., Gates, K.P., Barske, L., Wang, G., Lancman, J.J., Zeng, X.-X.I., Groff, M., Wang, K., Parsons, M.J., Crump, J.G., et al. (2017). Endoderm Jagged induces liver and pancreas duct lineage in zebrafish. *Nat. Commun.* 8, 769. 10.1038/s41467-017-00666-6.

695 40. McCright, B., Lozier, J., and Gridley, T. (2002). A mouse model of Alagille syndrome: Notch2 as a genetic modifier of Jag1 haploinsufficiency. *Development* 129, 1075–1082. 10.1242/dev.129.4.1075.

698 41. Ober, E.A., and Lemaigre, F.P. (2018). Development of the liver: Insights into organ and tissue morphogenesis. *J. Hepatol.* 68, 1049–1062. 10.1016/j.jhep.2018.01.005.

700 42. Thestrup, M.I., Caviglia, S., Cayuso, J., Heyne, R.L.S., Ahmad, R., Hofmeister, W., Satriano, L., Wilkinson, D.G., Andersen, J.B., and Ober, E.A. (2019). A morphogenetic EphB/EphrinB code controls hepatopancreatic duct formation. *Nat. Commun.* 10, 5220. 10.1038/s41467-019-13149-7.

704 43. Waddell, S.H., Yao, Y., Olaizola, P., Walker, A., Jarman, E.J., Gournopanos, K., Grdinaru, A., Christodoulou, E., Gautier, P., Boerrigter, M.M., et al. (2023). A TGF $\beta$ -ECM-integrin signaling axis drives structural reconfiguration of the bile duct to promote polycystic liver disease. *Sci. Transl. Med.* 15, eabq5930. 10.1126/scitranslmed.abq5930.

709 44. Wang, W., Pottorf, T.S., Wang, H.H., Dong, R., Kavanaugh, M.A., Cornelius, J.T., Dennis, K.L., Apte, U., Pritchard, M.T., Sharma, M., et al. (2021). IFT-A deficiency in juvenile mice impairs biliary development and exacerbates ADPKD liver disease. *J. Pathol.* 254, 289–302. 10.1002/path.5685.

713 45. Kopp, J.L., Dubois, C.L., Schaffer, A.E., Hao, E., Shih, H.P., Seymour, P.A., Ma, J., and Sander, M. (2011). Sox9+ ductal cells are multipotent progenitors throughout development but do not produce new endocrine cells in the normal or injured adult pancreas. *Development* 138, 653–665. 10.1242/dev.056499.

717 46. Dahl-Jensen, S.B., Yennek, S., Flasse, L., Larsen, H.L., Sever, D., Karremore, G., Novak, I., Sneppen, K., and Grapin-Botton, A. (2018). Deconstructing the principles of ductal network formation in the pancreas. *PLoS Biol.* 16, e2002842. 10.1371/journal.pbio.2002842.

721 47. Chen, S.-Y., and Liu, F.-C. (2023). The Fgf9-Nolz1-Wnt2 axis regulates morphogenesis of the lung. *Development* 150. 10.1242/dev.201827.

723 48. Zhang, K., Yao, E., Lin, C., Chou, Y.-T., Wong, J., Li, J., Wolters, P.J., and Chuang, P.-T. (2020). A mammalian Wnt5a-Ror2-Vangl2 axis controls the cytoskeleton and confers cellular properties required for alveogenesis. *eLife* 9. 10.7554/eLife.53688.

726 49. Cheong, S.-S., Akram, K.M., Matellan, C., Kim, S.Y., Gaboriau, D.C.A., Hind, M., Del Río Hernández, A.E., Griffiths, M., and Dean, C.H. (2020). The planar polarity component VANGL2 is a key regulator of mechanosignaling. *Front. Cell Dev. Biol.* 8, 577201. 10.3389/fcell.2020.577201.

730 50. Weng, S., Huebner, R.J., and Wallingford, J.B. (2022). Convergent extension requires  
731 adhesion-dependent biomechanical integration of cell crawling and junction  
732 contraction. *Cell Rep.* 39, 110666. 10.1016/j.celrep.2022.110666.